A&A 454, 453–458 (2006)
DOI: 10.1051/0004-6361:20064860

Astronomy & Astrophysics

A multi-wavelength study of the IRAS Deep Survey galaxy sample

I. Optical observations. The redshift distribution⋆

A. della Valle[1,2], P. Mazzei[1], D. Bettoni[1], H. Aussel[3,4], and G. De Zotti[1]

[1] INAF – Osservatorio Astronomico, Vicolo dell'Osservatorio 5, 35122 Padova, Italy
e-mail: [paola.mazzei;daniela.bettoni;gianfranco.dezotti]@oapd.inaf.it
[2] Dipartimento di Astronomia, Vicolo dell'Osservatorio 3, 35122 Padova, Italy
[3] Institute for Astronomy, 2680 Woodlawn Dr., Honolulu, 96800 Hawaii, USA
[4] AIM, UMR 7158, CE-Saclay, Bât 709, 91191 Gif-sur-Yvette, France

Received 16 January 2006 / Accepted 27 February 2006

ABSTRACT

Context. The IRAS Deep Survey (IDS) of the North Ecliptic Pole region remains one of the deepest complete far-infrared-selected galaxy samples available. ISOCAM observations in the LW3 filter (12−18 μm) of $3\farcm2 \times 3\farcm2$ fields centered on the nominal positions of 94 out of the 98 IDS sources yielding 116 ISOCAM detections. The resulting sample has allowed us to assess the source reliability, identify confusion effects, and pinpoint optical counterparts.
Aims. To fully exploit the potential of this sample for investigating galaxy evolution, we carried out optical observations of candidate identifications to 100 out of the 116 ISOCAM sources.
Methods. Optical imaging was acquired for 88 galaxies in 54 IDS fields: 44 galaxies were imaged in both the *B*- and the *R*-band, 33 only in the *R*-band, and 11 only in the *B*-band. These observations aimed at extending the MIR/FIR spectral energy distribution to the optical region and achieving morphological information. In addition, spectra were obtained for 65 IDS fields, 20 of which had not been observed before. Redshifts were measured for the 85 galaxies found within the positional error circles of 77 ISOCAM sources detected in those IDS fields.
Results. These observations allowed us to acquire spectroscopic redshifts of all counterparts that until now lacked them, so that, in combination with the results by Ashby et al. (1996), we now have redshifts for all IDS/ISOCAM galaxies in the field and, in particular, for the complete sub-sample of IDS galaxies defined by Mazzei et al. (2001).
Conclusions. In several cases we find evidence of multiple galaxies with very close redshifts within the error circles around ISOCAM positions, hinting at an important role for interactions in triggering the star formation activity. Although the z distribution of the complete sub-sample has a tail extending up to $z \simeq 0.37$, our results are inconsistent with the extreme cosmological evolution advocated by some models.

Key words. methods: observational – techniques: photometric – techniques: spectroscopic – galaxies: distances and redshifts – galaxies: photometry – galaxies: evolution

1. Introduction

The IRAS Deep Survey (IDS) sample was defined by co-adding IRAS scans of the North Ecliptic Polar Region (NEPR), representing more than 20h of integration time (Hacking & Houck 1987). It comprises 98 sources with $S(60\ \mu\mathrm{m}) > 50$ mJy over an area of 6.25 square degrees, although Mazzei et al. (2001) found it to be complete only for $S(60\ \mu\mathrm{m}) \geq 80$ mJy. It is still one of the deepest complete far-IR selected samples available. For comparison, the deep ISOPHOT surveys, FIRBACK at 170 μm (Puget et al. 1999; Dole et al. 2001), and ELAIS at 90 μm (Oliver et al. 2000) are all complete down to about 100 mJy. Moreover, the 70 μm Spitzer catalogue of the 8.75 sq. deg. Bootes field is flux limited to 80 mJy (Dole et al. 2004) and the Spitzer extragalactic "main" First Look Survey, covering about 4 sq. deg., is complete to about 20 mJy at 70 μm (cf. Fig. 2 of Frayer et al. 2006), but redshift measurements are available for a substantial fraction of sources (yet only 72%) merely for $S_{70\ \mu\mathrm{m}} > 50$ mJy.

The ASTRO-F space mission, also known as the InfraRed Imaging Surveyor (IRIS), will map the entire sky in four far-IR bands, from 50 to 200 μm, and two mid-IR bands, at 9 and 20 μm, with far-IR angular resolutions of 25−45 arcsec, reaching a detection limit of 44 mJy (5σ sensitivity) in the 50−75 μm band (Pearson et al. 2004). With the ASTRO-F orbit, the integration time on the NEPR will be particularly high, and, correspondingly, the detection limit significantly deeper than average.

Aussel et al. (2000) carried out ISOCAM observations with the LW3 filter, centered at $\lambda_{\mathrm{eff}} = 14.3$ μm of 94 of the 98 IDS fields (the last 4 fields were not observed because of lack of observing time), with a typical detection limit of 2−3 mJy. Each ISOCAM field is $3.2 \times 3.2'$ wide. These measurements have allowed us to: i) assess the reliability of IRAS detections; ii) to identify confusion effects (multiple sources within the IRAS resolution element) thanks to the much better ISOCAM resolution ($6''$) compared to IRAS ($60''$ at 60 μm); iii) locate the sources much more accurately (the astrometric precision achieved is of $3\farcs25$, 1σ), thus greatly easing optical identifications.

The IDS sample is also superior to most of the other far-IR selected samples in the coverage of the spectral energy

⋆ Appendices are only available in electronic form at http://www.edpsciences.org

distribution (SED) of member galaxies. In fact, in addition to the ISOCAM and to the 60 μm fluxes, most of them also have 100 μm fluxes and several have 25 μm fluxes from IRAS. We exploited the ISOCAM positions to determine improved IRAS fluxes (Mazzei et al. 2001). VLA observations for a large fraction of these sources are also available (Hacking et al. 1989). As a further step towards a complete characterization of the SEDs of these galaxies, and of their morphology, we also obtained, and present in this paper, optical/near-IR imaging of a substantial subset of the sample.

Redshifts of 76 tentative identifications in 70 IDS fields were obtained by Ashby et al. (1996). Although our more precise ISOCAM positions indicate that seven of their identifications need to be revised (see Sect. 2), their work shows that the redshift distribution extends at least to a redshift of 0.25. According to some models (Franceschini et al. 1994; Guiderdoni et al. 1998; Devriendt & Guiderdoni 2000), some IDS sources are expected to be at substantially higher redshifts. Therefore, the complete redshift distribution of our sample, which we present here, provides an important test for galaxy evolution models.

The plan of the paper is the following. In Sect. 2 we describe our imaging, spectroscopic observations, and the data reduction. In Sect. 3 we present the redshift distribution of IDS sources. In Sect. 4 we summarize and discuss our main conclusions.

2. Observations and data reduction

Aussel et al. (2000) report ISOCAM/LW3 data (measured fluxes or upper limits) for 116 sources in the 94 3.2×3.2′ IDS fields that could be observed in the assigned time. We excluded 3 sources that turned out to be catalogued stars: 3-67A belongs to the BD Catalogue (Argelander 1903), 3-63B to the GSC (Guide Star Catalogue, Lasker 1998), and 3-94B is in the Tycho-2 Catalogue (Hog et al. 2000). One additional ISOCAM source (3-02A) was left out because it is more than 2σ (90″) away from the nominal position of the corresponding IRAS source.

We carried out imaging and/or spectroscopic observations of 100 of the remaining 112 ISOCAM sources. The 12 sources we missed had redshift measurements by Ashby et al. (1996) and were therefore given lower priority in our program.

Our highest priority targets were the 20 IDS fields not observed by Ashby et al. (1996) (3-10, 3-29, 3-31, 3-37, 3-38, 3-39, 3-44, 3-49, 3-53, 3-55, 3-57, 3-58, 3-59, 3-61, 3-64, 3-68, 3-72, 3-73, 3-79, and 3-91) and the 4 (3-24, 3-51, 3-86, and 3-89) for which no redshifts were reported, even though they were observed.

As for the other fields, we had some difficulty deciding whether the redshifts reported by Ashby et al. (1996) referred to our optical counterparts or not. In fact, Ashby et al. (1996) only give the nominal positions of the centers of the IDS field (Hacking & Houck 1987) plus some other positional indications (e.g., NE, SW, etc.) when the galaxy is off center. We therefore re-observed most of their fields, starting from those whose optical identifications were not completely unambiguous, but also aiming at obtaining a better spectroscopic and/or morphological characterization of as many IRAS/ISOCAM galaxies as possible.

The complete list of our targets is given in Table C.1. Following Aussel et al. (2000), multiple ISOCAM sources in a single IRAS field are labelled by a capital letter (A, B, ...), while multiple optical galaxies within an ISOCAM error circle (see Sect. 2.3) are labelled by adding a number (e.g. 3-04A1, 3-04A2; Col. 1). In Cols. 2 and 3 we give the coordinates, in Cols. 4 and 5 the spectroscopic and imaging observing runs (the corresponding setups are specified in Sects. 2.2 and 2.1), in Col. 6 our redshift measurements, and in Cols. 7 and 8 the R and B magnitudes with their errors. Finally, in Col. 9 we indicate whether or not (y/n) the galaxy belongs to the complete sample of 56 IDS sources with $S(60\ \mu\mathrm{m}) > 80$ mJy defined by Mazzei et al. (2001).

The redshift values are generally very accurate (see Sect. 2.2). The exceptions are the 4 galaxies without strong emission lines. Their redshift estimates are identified by a "*".

2.1. Imaging observations

Our program of optical imaging observations in B and R bands was carried out from 2000 to 2002. We acquired both B- and R-band imaging of 44 galaxies in the fields around 37 ISOCAM sources detected in 28 IDS fields. Imaging only in the R-band was obtained for 33 galaxies within the error boxes of 26 additional ISOCAM sources in 21 IDS fields. Moreover, we have images only in the B-band of 11 galaxies, candidate counterparts to 5 additional ISOCAM sources in 5 IDS fields.

On the whole, we have imaged 88 galaxies in the fields around the 68 ISOCAM sources found in 54 IDS fields, selected on the basis of two distinct criteria. Sometimes we needed to pin down the most likely counterpart to IRAS/ISOCAM sources. On the other hand, in the case of relatively bright galaxies, observations were aimed at investigating the morphology and the environment of the optical identifications, as well as at extending the coverage of their SEDs; we will describe the results of our investigations of these issues in a forthcoming paper (Bettoni et al. 2006). Most observations were performed at the 3.5 m Telescopio Nazionale Galileo (TNG) equipped with DOLORES or OIG; 5 sources were observed using the 10 m Keck II telescope with the Echellette Spectrograph and Imager (ESI).

Only for runs #1, #4 and #5 were the nights photometric. For the two non photometric nights, we derived photometric zero point shifts by comparing standard stars in fields in common with photometric nights. DOLORES was equipped with a Loral-thinned and back-illuminated 2048 × 2048 CCD with a scale of 0.275″ pixel^{-1} and a field of view of 9.4 × 9.4 arcmin. The OIG was equipped with a mosaic of two thinned and back-illuminated EEV 42-80 CCDs, each with 2048 × 4096 pixels. The pixel size and pixel scale are of 13.5 μm and 0.072″ pixel^{-1}, respectively, corresponding to a total field of view of about 4.9′×4.9′. The OIG data were resampled with a binning of two, corresponding to a spatial scale of 0.144″/pixel. Exposure times were 300 s and 1800 s in R and B filters, respectively.

At Keck II we used ESI in "direct image" mode with an unvignetted field of 2′ × 8′. The detector was an MIT-Lincoln Labs CCD with 2048 × 4096 pixels of 15 μm for a pixel scale of 0.153″ pixel^{-1}. Observations were carried out using the Johnson B filter (2′ × 3.5′ field of view) and the $\mathcal{R}$ filter with a field of view of 2′ × 8′. Exposure times were 180 s in both filters, except for sources 3-83A (B and R) and 3-89A (R) for which we used 120 s.

During the observations, three sequences of photometric standard stars (Landolt 1992) were taken in B, V, and R filters. At least 3 sky flat-fields per filter and 10 bias were taken at the beginning and at the end of each night of observation. Data were reduced using the standard IRAF reduction packages. Scientific and calibration frames were bias subtracted and divided for flat-field. The photometric calibration was done using the IRAF *digiphot* package (see Appendices A and B for more details). Galactic extinction was accounted for using the dust maps by Schlegel et al. (1998). Total magnitudes of the

galaxies were measured with *galfit* (Peng et al. 2002). This package, which convolves the image with the PSF to minimize the broadening effect of the seeing, allows a two-component fit (disk and bulge) of the galaxy profile, deconvolved from the PSF. Thus it provides detailed information on the morphological properties of the galaxies which will be presented in a forthcoming paper (Bettoni et al. 2006).

The limiting magnitude for a point source with the TNG telescope is 23.0 in the B band (with exposure time of 1800s) and 21.5 in the R band (exposure time of 300s). The point source limiting magnitudes for the KeckII images are ∼24.8 in B and ∼22.6 in R with an exposure time of 180s.

We could not calibrate images in the ESI $\mathcal{R}$ filter yet, so the magnitudes of the 12 galaxies and 1 star detected (3-44A1,2,3, 3-53A1,2,3,4, 3-65A1,2, 3-83A1,2, 3-89A1,2) in that filter are not yet available. Source 3-44A3 was not detected in the B band.

Nine of the potential counterparts to ISOCAM sources, 3-01A, 3-17A, 3-18A, 3-19B, 3-33B, 3-79B, 3-80A, 3-88B, 3-92B, show a stellar PSF luminosity profile and are therefore classified as stars. The last 4 are listed in the Tycho-2 star Catalogue (Hog et al. 2000).

2.2. Spectroscopic observations

The optical spectroscopy was carried out from 2000 to 2003 using different telescopes: the Asiago Cima Ekar 1.82 m telescope, the TNG, and the Keck II telescope, which was appropriate given the magnitude of the target.

Spectroscopic observations were made for 90 optical sources in 65 IDS fields. For 41 of them redshift measurements were reported by Ashby et al. (1996). They were re-observed either because it was not clear whether the published redshifts referred to our optical counterparts, or to characterize the source spectra. Four additional fields were observed by Ashby et al., but no redshifts were reported, and 20 IDS fields had not been previously observed. No sources were detected by Aussel et al. (2000) in 4 IDS fields (3-06, 3-22, 3-87, and 3-95), while in three additional fields (3-01, 3-02, and 3-18) ISOCAM sources are found well outside the IRAS error circles (and in the cases of 3-01 and 3-18, ISOCAM sources turn out to be stars); these 7 sources were not observed spectroscopically. For the remaining 22 out of the 94 IDS/ISOCAM fields, we have adopted the redshifts measured by Ashby et al. (1996). We obtained 85 new redshift estimates of possible counterparts to 81 ISOCAM sources listed by Aussel et al. (2000) (in several cases our optical images show more than one galaxy within the ISOCAM error circle (see Sect. 2.3)). Four additional possible counterparts turned out to have spectra typical of stars, in addition to the 9 classified as stars on the basis of our images.

With the Cima Ekar telescope, the Asiago Faint Object Spectrograph and Camera (AFOSC, Desidera et al. 2003) was used with grisms #4 and #8 and a 2.″1 wide slit with both grisms, corresponding to an instrumental velocity resolution of 470 km s^{-1} for grism #4 and of 190 km s^{-1} for grism #8 at the Hα line. The wavelength coverage is 3350−7750 Å and 6250−8050 Å, the dispersion 4.3 Å pixel^{-1} and 1.8 Å pixel^{-1}, respectively. The detector is a CCD Tektronix TK 1024 × 1024, with pixel size 24 μm, corresponding to a spatial scale along the slit of 0.473″ pixel^{-1}.

With the TNG telescope, we used DOLORES with the LR-R grism, which provides a wavelength coverage from 4470 Å to 10 360 Å and a resolution of 2.9 Å pixel^{-1}. The detector is a Loral CCD 2048 × 2048 with pixel size 15 μm, and a spatial scale of 0.275″ pixel^{-1}. We used a long-slit 1.5″ wide. This setup provides an instrumental velocity resolution of ∼300 km s^{-1} at the wavelength of the Hα line. Exposure times ranged from 600 to 1800s.

For the observations with the Keck II, we used ESI in the *echelle mode* in order to obtain high-resolution spectra. The wavelength coverage goes from 3900 to 11 000 Å across 10 echelle orders (from order 6, the reddest one, to order 15, the bluest one). The dispersion ranges between 0.16 Å pixel^{-1} in the blue region to 0.30 Å pixel^{-1} in the red one. The instrumental *FWHM* is 11.5 km s^{-1} pixel^{-1}, the same in all orders. The detector, a 2048×4096 MIT-Lincoln Labs CCD with pixel size 15 μm, provides a spatial scale along the slit from 0.168 arcsec pixel^{-1} in the red to 0.120 arcsec pixel^{-1} in the blue region. Spectra were obtained with a 1.0″ × 20″ wide slit, corresponding to an instrumental velocity resolution of 35 km s^{-1} at the Hα line.

The mean *S/N* ratio for the Asiago data is ≃10, for the TNG observations is ≃25, for the blue region of the Keck II ≃10, and for the red region of the Keck II ≃15. The slit was normally oriented along the North-South direction. However, if two targets were close enough, it was oriented so as to obtain the spectra of both (9 cases) simultaneously. All the spectra were bias and flat-field corrected, trimmed, and wavelength calibrated. Flux calibration was based on spectrophotometric standard stars (Oke 1990), and radial velocity stars were observed each night with the same setup as for our targets. For the reduction of the Keck+ESI spectra we followed the procedure used by Geha et al. (2002). More details on spectra reduction are given in Appendix C. The good spatial resolution of the ESI spectra allows us to measure the rotation curves for almost all the galaxies (31) observed; the results will be presented in a subsequent paper (Bettoni et al. 2006).

2.2.1. Emission lines and redshifts

All but four (3-13A, 3-32B, 3-57A2, 3-68A) galaxies in the sample show strong emission lines: [O II] 3727 Å, Hβ, [O III] 4959 Å, [O III] 5007 Å, Hα, [N II] 6548-6583 Å, and [S II] 6717−6731 Å.

The spectrum of 3-32B shows only a weak Hα emission. In the spectra of the galaxies 3-13A, 3-57A2, and 3-68A, we identified only the absorption feature of Mg I at 5200 Å that we used to derive the redshift. The redshift estimates of these 4 galaxies are labelled by a "*" in Table C.1 (see Sect. 2). The low sensitivity of the L-LR grism (TNG) in the blue spectral region did not allow us to detect "green lines". Moreover, the region $\lambda > 8600$ Å is contaminated by strong telluric bands (Osterbrock 1996). Note that none of these sources belong to the complete sub-sample (Mazzei et al. 2001), although 3-57A2 may be a companion of 3-57A1, which we identify as the counterpart of the IRAS source 3-57 that is in the complete sub-sample.

Spectra were classified on the basis of the presence or absence of various emission lines after correcting for Galactic extinction, following Schlegel et al. (1998), and for underlying stellar continuum (more details will be presented in Bettoni et al. 2006).

In order to measure the redshift, we used the IRAF task *emsao* to find the emission lines in the spectrum and then to compare their central wavelengths with suitable template tables. The typical uncertainty on redshift estimates is $\delta z \lesssim 0.0001$.

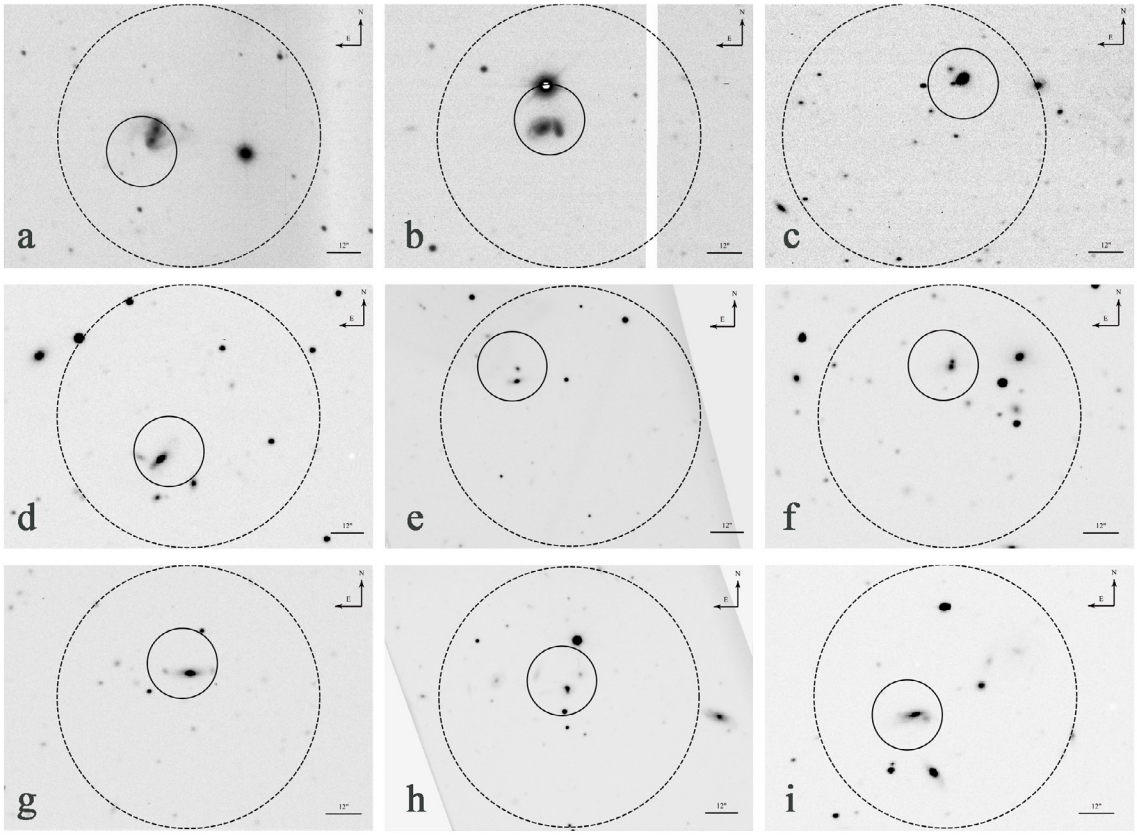

Fig. 1. *R* imaging of ISOCAM sources 3-04A **a)**, 3-10A **b)**, 3-33A **c)**, 3-39A **d)**, 3-44A **e)**, 3-49A **f)**, 3-51A **g)**, 3-53A **h)**, and 3-54A **i)**. Here and in the following figure, the small circle encompasses an area of 12″ radius centered on the nominal position of the IDS/ISOCAM source, and the larger one an area of 45″ radius centered on the nominal position of the IDS/IRAS source. Each panel has a size of 127″ × 90″.

2.3. Multiple optical counterparts

We define as ISOCAM sources with multiple candidate optical counterparts those sources with more than one source detected in our *B*-and/or *R*-band images within 12″ from the nominal position of the ISOCAM source (12″ correspond to a 2σ positional uncertainty). On the whole, we have 17 such sources totaling 37 possible counterparts. We measured redshifts for 25 of them; the remaining ones are either too faint or have been discovered after the spectroscopic run in their field. A short description of these multiple counterparts is given below.

3-04A. In Fig. 1a we see two galaxies with approximately the same redshift ($z \simeq 0.118$). They are very close to each other (angular separation of about 4″); tails, tracers of interaction, are also visible. Ashby et al. (1996) report a single redshift of 0.121 for this IRAS field.

3-10A. (Fig. 1b) two galaxies with similar redshifts and *R* magnitudes are visible.

3-33A. (Fig. 1c) there are three very faint galaxies within the error circle. We measured the redshift only of the brightest one; it almost coincides with the one measured by Ashby et al. (1996) ($z = 0.1440$).

3-39A. (Fig. 1d) two galaxies are visible in the *R* image; we only measured the redshift of the brighter one.

3-44A. (Fig. 1e) there are three galaxies within the error circle. We measured different redshifts for the two brighter ones; the third galaxy is projected on the outer regions of the brightest galaxy.

3-49A. (Fig. 1f) two galaxies are visible in the *R* image; we only measured the redshift of the brighter one.

3-51A. (Fig. 1g) we measured the redshift of the edge-on spiral ($z = 0.1108$); two fainter companions at the opposite sides of its major axis are also visible. Ashby et al. (1996) report a much lower redshift ($z = 0.0259$).

3-53A. (Fig. 1h) there are three galaxies and a star inside the error circle. We measured the redshift of the brightest galaxy (which is also the closest to the center of the circle); it has a very disturbed morphology and could be interacting with a fainter galaxy superimposed on its image.

3-54A. (Fig. 1i) the two galaxies we see may be interacting; we measured the redshift of the brighter one. Ashby et al. (1996) report a very similar redshift, 0.0799.

3-57A. (Fig. 2a) there are two galaxies within the error circle. No emission lines are visible in the spectrum of the faintest one, but we detect one absorption feature that may be identified as 5200 Å Mg I at the same redshift as the companion galaxy.

3-59A. (Fig. 2b) this is a very disturbed, perhaps interacting, galaxy.

3-65A. (Fig. 2c) we see two galaxies with a very similar redshift, $z \simeq 0.167$. Ashby et al. (1996) give a single, slightly different, redshift, 0.173, for this IRAS field.

3-78C. (Fig. 2d) three galaxies are visible in our image. We measured the redshifts of two of them, which turned out to be very close to each other. Asbhy et al. (1996) report only one redshift for the 3-78 field, 0.0774, which agrees with that of our IDS/ISOCAM source 3-78B (0.0781), which we also adopt as the counterpart to the IRAS source.

3-83A. (Fig. 2e) we have two galaxies with the same redshift. Three optical sources (East, West, North) are listed by Asbhy et al. (1996) who, however, report only two redshifts for the East

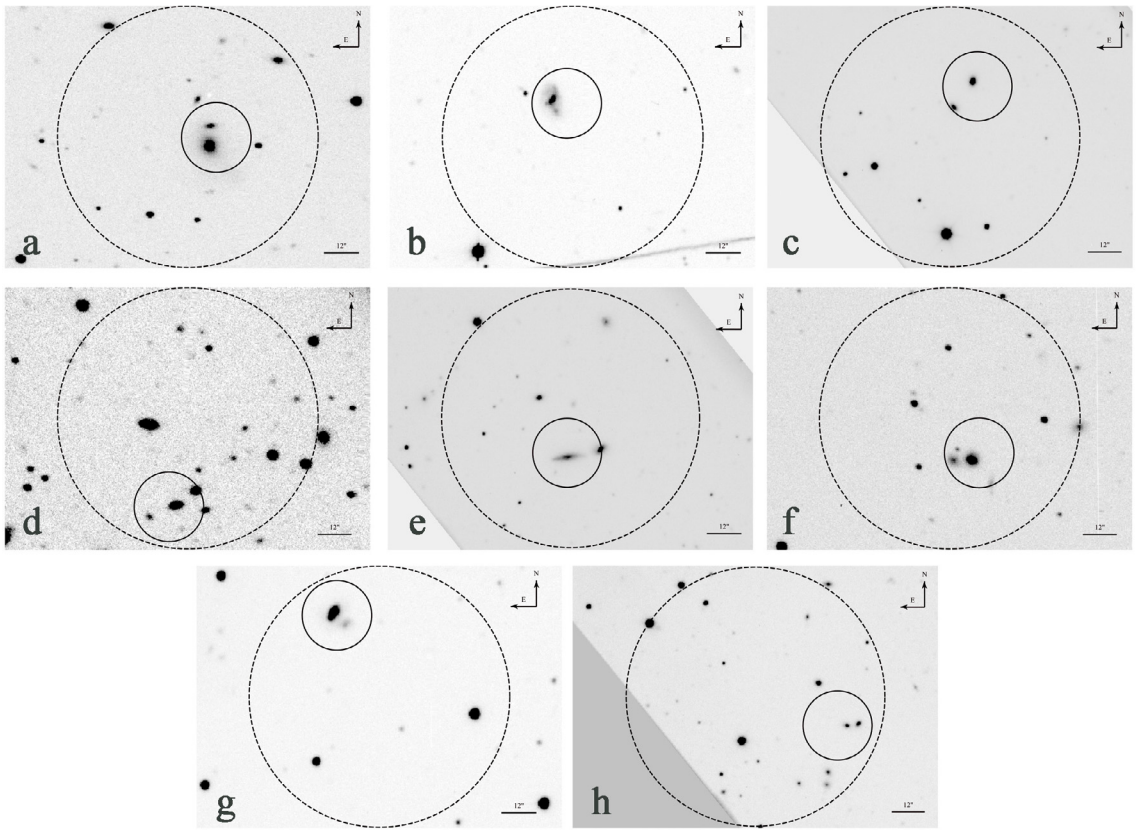

Fig. 2. *R* imaging of the ISOCAM sources 3-57A **a)**, 3-59A **b)**, 3-65A **c)**, 3-78C **d)**, 3-83A **e)**, 3-85A **f)**, 3-88A **g)**, and 3-89A **h)**.

and West galaxies, which turn out to be equal (0.107) and coincide with ours.

3-85A. (Fig.2f) we measured the redshift of the brighter of the two galaxies seen within the error circle. Our result agrees with that given by Ashby et al. (1996).

3-88A. (Fig. 2g) we measured the redshift of the brighter of the two galaxies seen within the error circle. Ashby et al. (1996) report almost the same redshift value, 0.0519.

3-89A. (Fig. 2h) the two galaxies seen have almost equal redshifts.

3. Redshift distribution

As mentioned in Sect. 1, the redshift distribution is particularly important for testing evolutionary models. In Fig. 3 (left-hand panel) we show it for the complete sample of 56 sources with $S(60\ \mu\mathrm{m}) > 80$ mJy defined by Mazzei et al. (2001). As discussed in Sect. 2.3, there are multiple optical galaxies within the ISOCAM error circle in several cases. However, for such a sample, galaxies turned out to have similar redshifts (Table C.1), so we adopted their mean value as the redshift of the IDS source.

The NEPR supercluster found by Ashby et al. (1996; see also Burg et al. 1992, and Mullis et al. 2001) dominates the z-distribution between 0.08 and 0.09. Other peaks are visible in the redshift ranges between 0.02 and 0.03, 0.05, and 0.06, and between 0.11 and 0.12.

Figure 3 (right panel) shows the cumulative redshift distributions of optical counterparts of different far-IR selected samples discussed in this work. A Kolmogorov-Smirnov (K-S) two-sample test shows that there is a 98% probability that the redshift distribution of the 56 IDS/ISOCAM sources belonging to the 60 μm complete sample by Mazzei et al. (2001), which includes 17 identifications by Ashby et al. (1996), is drawn from the same parent distribution as the sample of 76 IRAS galaxies whose redshifts were measured by Ashby et al. (1996). The probability that the Ashby sample is drawn from the same parent distribution as the sample of 85 IDS/ISOCAM galaxies with measured redshifts (including 22 redshifts from Ashby et al. 1996), is 59%.

About 70% of IDS/ISOCAM galaxies are at $z < 0.1$, 19% at $0.1 \le z \le 0.2$, and 11% galaxies at $z > 0.2$. The redshift distribution extends beyond the maximum redshift measured by Ashby et al. (1996), although, as shown by the K-S test, the difference in the two distributions is not statistically significant, as expected given the small number of sources in the high-z tail. However, the high-z tail is not as populated as predicted by some evolution models. Implications for the 60 μm local luminosity function and its evolution will be discussed in a forthcoming paper (Mazzei et al. 2006).

4. Discussion and conclusions

We carried out spectroscopic and imaging observations of candidate optical counterparts to ISOCAM sources detected by Aussel et al. (2000) in $3\farcm2 \times 3\farcm2$ fields centered on the nominal positions of 94 out of the 98 sources in the IRAS Deep Survey (IDS) sample by Hacking & Houck (1987). ISOCAM observations have allowed an assessment of the reliability of IDS sources and a much more precise location of the confirmed ones.

We obtained optical images and/or spectra of the 100 ISOCAM sources detected by Aussel et al. (2000) in 77 IDS fields, out of the total of 116 sources found in the 94 IDS fields (in 9 of which however no ones ISOCAM sources were detected, even doubtful). The 16 sources we did not observe include 3 stars, a source outside the IRAS error box and 12 galaxies with redshift measurements by Ashby et al. (1996).

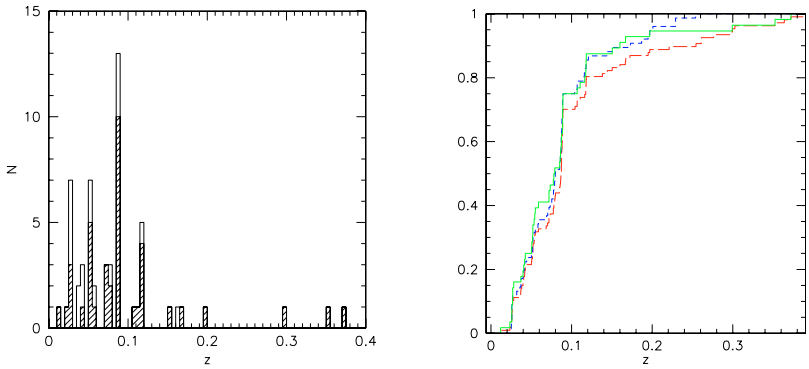

Fig. 3. Redshift distribution of our far-IR selected complete sample comprising 56 sources with $S(60\,\mu\mathrm{m}) > 80$ mJy (*left-hand panel*). Seventeen redshift measurements come from Ashby et al. (1996) and the barred histogram shows our data, including 23 redshifts in common with Ashby et al. The right-hand panel shows, for comparison, the cumulative redshift distribution of different samples: continuous line for optical counterparts of the IDS/ISOCAM complete sample by Mazzei et al. (2001), long-dashed line for optical counterparts of the IDS/ISOCAM sample by Aussel et al. (2000), and the short-dashed line for the IDS sample by Ashby et al. (1996).

As discussed in Table C.1, we acquired optical imaging of the fields around 68 ISOCAM sources (37 in both the *B* and *R* bands, 26 only in the *R* band, and 5 only in the *B* band), found in a total of 54 IDS fields. Nine ISOCAM sources were identified as stars on the basis of optical images. We measured *B* magnitudes for 55 galaxies and *R* magnitudes for 77; 44 of these galaxies have both *R* and *B* magnitudes. The total number of galaxies for which we obtained at least one magnitude measurement is 88.

While Aussel et al. (2000) found evidence of strong confusion effects, i.e. of multiple ISOCAM sources contributing to the IRAS flux in 4 IDS fields, our optical images show that two or more galaxies with very close redshifts may contribute to the ISOCAM flux in at least 7 cases (3-04A, 3-10A, 3-57A, 3-65A, 3-78C, 3-83A, 3-89A). This brings in the role of interactions in triggering starbursts and, perhaps, nuclear activity, which will be discussed in a forthcoming paper (Bettoni et al. 2006).

We carried out spectroscopic observations of 90 optical sources found within the error circles of 77 ISOCAM sources in 65 IDS fields. Redshifts were measured for 85 galaxies, including 41 for which redshifts were previously reported by Ashby et al. (1996).

Combining our observations with those by Ashby et al. (1996), we have reliable identifications and spectroscopic redshifts for 100% of the complete sub-sample comprising 56 sources with $S(60\,\mu\mathrm{m}) > 80$ mJy (Mazzei et al. 2001). Redshifts of 17 sources come from Ashby et al., and 16 are new; for the other 23 galaxies we confirm the Ashby results. The redshift distribution shows a tail extending up to $z \simeq 0.37$, while the maximum redshift measured by Ashby et al. (1996) is 0.25. A K-S test shows, however, that the difference in the redshift distributions is not statistically significant. According to some models (Franceschini et al. 1994; Guiderdoni et al. 1998; Devriendt & Guiderdoni 2000), some IDS sources may be at substantially higher redshifts. Therefore, the complete redshift distribution of our sample we present here provides an important test of galaxy evolution models and can provide interesting constraints on the evolution of the luminosity function. A detailed discussion of this issue will be presented in a forthcoming paper (Mazzei et al. 2006).

Finally, we note that 15 of our ISOCAM sources have been identified as stars. Eight of them have 14.3 μm flux above the 5σ detection limit of 3.5 mJy (see Aussel et al. 2000), in excellent agreement with the prediction (7.5 sources in the surveyed area of $\simeq 0.2\,\mathrm{deg}^2$) for the model of Franceschini et al. (2001).

Acknowledgements. We thank the referee, M. Ashby, for an unusually helpful and quick report. Work supported in part by MIUR (Ministero Italiano dell'Università e della Ricerca) and ASI (Agenzia Spaziale Italiana). IRAF (`http://iraf.noao.edu`) is distributed by the National Optical Astronomy Observatories, which are operated by the Association of Universities of Research in Astronomy Inc., in agreement with the National Science Foundation

References

Argelander, F. W. A. 1903 (Bonn: Marcus and Weber's Verlag)
Ashby, M. L. N., Hacking, P. B., Houck, J. R., et al. 1996, ApJ, 456, 428
Aussel, H., Coia, D., Mazzei, P., De Zotti, G., & Franceschini, A. 2000, A&AS, 141, 257
Bettoni, D., Della Valle, A., Mazzei, P., et al. 2006, in preparation
Devriendt, J. E. G., & Guiderdoni, B. 2000, A&A, 363, 851
Burg, R., Giacconi, R., Huchra, J., et al. 1992, A&A, 259, L9
Desidera, S., Fantinel, D., Giro, E., & Navasardyan, H. 2003, in AFOSC User Manual, internal report,
`www.pd.astro.it/Asiago/5000/5100/man01_2.ps.gz`
Dole, H., Gispert, R., & Lagache, G. 2001, A&A, 372, 364
Dole, H., Le Floc'h, E., Pérez-González, P. G., et al. 2004, ApJS, 154, 87
Franceschini, A., Toffolatti, L., Mazzei, P., Danese, L., & de Zotti, G. 1991, A&AS, 89, 285
Franceschini, A., Mazzei, P., De Zotti, G., & Danese, L. 1994, ApJ, 427, 140
Frayer, D. T., Fadda, D., Yan, L., et al. 2006, AJ, 131, 250
Freeman, K. C. 1970, ApJ, 160, 811
Geha, M., Guhathakurta, P., & Van der Marel, R. P. 2002, AJ, 124, 3073
Guiderdoni, B., Hivon, E., Bouchet, F. R., & Maffei, B. 1998, MNRAS, 295, 877
Hacking, P., Beichman, C. A., Condon, J. J., & Houck, J. R. 1989, ApJ, 339, 12
Hacking, P., & Houck, J. R. 1987, ApJS, 63, 311
Ho, L. C., Filippenko, A. V., & Sargent, W. L. W. 1997, ApJS, 112, 315
Hog, E., Fabricius, C., Makarov, V. V., et al. 2000, A&A, 355, L27
Landolt, A. U. 1992, AJ, 104, 340
Lasker, B. M. 1998, Bull. Am. Astron. Soc., 30, 912
Mazzei, P., & Curir, A. 2003, ApJ, 591, 784
Mazzei, P., Xu, C., & De Zotti, G. 1992, A&A, 256, 45
Mazzei, P., De Zotti, G., & Xu, C. 1994, ApJ, 422, 81
Mazzei, P., Aussel, H., Xu, C., et al. 2001, New Astr., 6, 265
Mazzei, P., Della Valle, A., Bettoni, D., et al. 2006, in preparation
Mullis, C. R., Henry, J. P., Gioia, I. M., et al. 2001, ApJ, 553, L115
Oke, J. B. 1990, AJ, 99, 1621
Oliver, S., Rowan-Robinson, M., & Alexander, D. M. 2000, MNRAS, 316, 749
Osterbrock, D. E. 1996, Space Sci. Rev., 75, 610
Pearson, C. P., Shibai, H., Matsumoto, T., et al. 2004, MNRAS, 347, 1113
Peng, C. Y., Ho, L. C., Impey, C. D., & Rix, H. 2002, AJ, 124, 266
Puget, J.-L., Lagache, G., Clements, D., et al. 1999, A&A, 345, 29
Rousselot, P., Lidman, C., Cuby, J.-G., Moreels, G., & Monet, G. 2000, A&A, 354, 1134
Sandage, A., Binggeli, B., & Tamman, G. M. 1985, AJ, 90, 1759
Sheinis, A. I., Bolte, M., Epps, H. W., et al. 2002, PASP, 114, 851
van Dokkum, P. G. 2001, PASP, 113, 1420

Online Material

Appendix A: Imaging reduction

Imaging data reduction was performed using the standard IRAF routines. Sky flat-field and bias images were combined, and scientific and calibration frames were bias-subtracted and flat-fielded. For the ESI instrument we used the same task as used for the spectroscopic reductions (see Appendix C), written by Gregory D. Wirth (Keck staff).

The images of the objects with two frames were combined after alignment. They were usually observed in succession, so that the misalignment and the rotation could be disregarded.

The airmass was calculated for both scientific and calibration frames using time and telescope position data written in the header of the images. The photometric calibration was made using the IRAF `digiphot` package. Instrumental magnitudes of standard stars were measured with the same aperture (7″) as used by Landolt (1992). The values obtained were used to compute, for each night and each instrument, a set of color curve equations of the form:

$$\begin{aligned} B &= b + zp^{B}_{BV} + C^{B}_{BV}\cdot(B-V) + k_B\cdot X \\ V &= v + zp^{V}_{BV} + C^{V}_{BV}\cdot(B-V) + k_V\cdot X \\ R &= r + zp^{R}_{VR} + C^{R}_{VR}\cdot(V-R) + k_R\cdot X \end{aligned} \tag{A.1}$$

$$\begin{aligned} B &= b + zp^{B}_{BR} + C^{B}_{BR}\cdot(B-R) + k_B\cdot X \\ R &= r + zp^{R}_{BR} + C^{R}_{BR}\cdot(B-R) + k_R\cdot X \end{aligned} \tag{A.2}$$

$$R = r + zp_R + k_R\cdot X \tag{A.3}$$

where b, v and r are the instrumental magnitudes, $C^{\rm fil}_{\rm col}$ is the color term of the calibration of the filter fil against the color col, $zp^{\rm fil}_{\rm col}$ the corresponding zero point, k_λ the extinction coefficient, and X the air-mass. We used Eqs. (A.1) to find the coefficients for the three colors B, V, and R in order to compare our results with the standard values of the telescope. Using Eqs. (A.2) we derived the coefficients to calibrate the fields observed both with B and R filters, while the images taken in run #3, when only the R filter was used, were calibrated with Eq. (A.3). We calculated the atmospheric extinction coefficient k_λ only for runs #3 and #5, for which we had an adequate number of standard fields. Because our measured coefficients agree with those of the telescope, we used them in the remaining runs.

In Table A.1 we list the color coefficients for each night and each instrument used.

Appendix B: Astrometric calibration

The astrometric calibration of the images was performed in order to identify the optical counterparts of our IDS/ISOCAM sample. This is especially needed for analyzing the multiple optical counterparts (see Sect. 2.2.1) that could contribute to the IR flux. In general, the astrometric solution is a function, $f(x, y) = \alpha, \delta$, that associates the pixel coordinates x, y on the frame (*logical* coordinates) to the absolute sky coordinates α, δ (the *world* coordinates). Function f is a combination of both the geometric properties of the camera and the projection used to transform the spherical equatorial coordinate system into the flat surface of the CCD.

An astrometric solution is normally built by a direct comparison between the logical and the world position of as large a number of stars as possible. This implies that high precision catalogues must be used. We used the *Second Guide Star Catalogue* (GSC-II; Lasker 1998) with positional accuracy of 0.3−0.75″. For every field observed with TNG+LRS (9.4′ × 9.4′), there are generally more than 60 stars catalogued in the GSC-II, while there are only few stars (in some cases less than 10) for the fields observed with OIG and ESI. Since OIG is an array of two CCDs, each CCD is astrometrized independently.

To compute the astrometric solution, the IRAF `imcoord` package was used. The first step was to associate the logical coordinates of the objects to the world coordinates using a basic astrometric solution built with a reference point, the scale, and the orientation of the image. They were re-centered using a centroid algorithm and fitted using a set of Legendre polynomials. The order was set to 4 for the large DOLORES frames and to 2 for the ESI and OIG ones. The overall rms of the fit was on the order of 0.1″.

Appendix C: Spectroscopic reduction

AFOSC and DOLORES data were reduced using the IRAF long-slit spectral reduction tasks. Bias and flat-field images were added for every night. The scientific frames were corrected for bias and flat-field and then trimmed. Usually, an overscan region was used for bias correction but for frames of runs 2 and 7 in Table C.1, a bias image was used since the count level was not constant in the frame. Cosmic rays of individual exposures were subtracted with the LA_Cosmic task (van Dokkum 2001). For 4 objects, two spectra were obtained during the same night: in these cases cosmic rays were removed combining the frames using *imcombine* with *crreject* rejection and *average* type of combine after a check of the spectra alignment.

The frames were calibrated using arc-lamp spectra (Ne/Ar lamps for DOLORES LR-R grism, Ne/Hg-Cd and Ne/Th for AFOSC grism #4 and #8, respectively). The wavelength calibration was done in order to extract two-dimensional information from the spectra. After the identification of the lamps lines, these were re-identified across the dispersion axis. A two-dimensional map wavelength/pixel position was fitted and the spectra were finally calibrated and aligned across the dispersion axis. The rms of the residuals in the wavelength solution is less than 0.98 Å and less than 0.91 Å for the spectra taken with DOLORES and AFOSC, respectively. The goodness of the calibration was checked by measuring the wavelength of some sky lines. In some cases we measured a residual wavelength shift that was corrected. After this correction, the error measured with respect to the sky-line positions is less than 10 km s^{-1} for the DOLORES data and less than 50 km s^{-1} for the AFOSC ones.

Unidimensional spectra were extracted and sky-subtracted. For unresolved objects we extracted only one spectrum that included the whole source. Several unidimensional spectra were extracted for the spatially resolved ones: one in the nuclear region for the redshift measurement, the others at different offsets from the center for velocity gradient calculation. Unidimensional spectra of the whole sources were also extracted to measure the entire emission line flux. We also used the two-dimensional spectra for spatially resolved objects: these were obtained from the calibrated frames subtracting the sky.

We decided not to use the IDL task managed by the ESI staff to reduce the ESI spectra, but we followed the procedure used by Geha et al. (2002). Flat-field and bias frames were combined as described before. Since the ESI spectrograph CCD usually operates in dual-amplifier readout (each amplifier has different bias level and different gain), the *esibias* task written by Gregory D. Wirth (Keck staff) was used for overscan, bias, and trim corrections. A bad-pixel mask was created using a flat-field image to remove the bad columns in the up-left side of

Table A.1. Instruments set-up for each night of observations.

Night	Filter	Zero point	Color term	Extinction
		TNG + OIG		
Apr. 10, 2000	B vs. $(B-R)$	25.763	0.059	−0.25
	R vs. $(B-R)$	25.553	−0.065	−0.11
Apr. 12, 2000	B vs. $(B-R)$	25.769	0.074	−0.25
	R vs. $(B-R)$	25.543	−0.049	−0.11
May 9, 2000	B vs. $(B-R)$	25.805	0.064	−0.25
	R vs. $(B-R)$	25.525	−0.041	−0.11
Jun. 10, 2002	B vs. $(B-R)$	25.717 ± .066	0.166 ± .056	−0.27 ± .04
	R vs. $(B-R)$	25.546 ± .019	0.043 ± .003	−0.11 ± .01
		TNG + DOLORES		
Jun. 20, 2000	R	26.423 ± .041	–	−0.13 ± .03
Jun. 9, 2002	B vs. $(B-R)$	26.376 ± .031	0.028 ± .005	−0.31 ± .02
	R vs. $(B-R)$	26.306 ± .017	0.011 ± .003	−0.18 ± .01
Jun. 10, 2002	B vs. $(B-R)$	26.292 ± .048	0.023 ± .008	−0.24 ± .04
	R vs. $(B-R)$	26.244 ± .019	0.011 ± .003	−0.11 ± .01
Jun. 11, 2002	B vs. $(B-R)$	26.278 ± 0.016	0.037 ± .004	−0.26 ± .01
	R vs. $(B-R)$	26.232 ± 0.023	0.004 ± .002	−0.13 ± .02
		KECKII + ESI		
Jul. 18, 2001	B	24.56	–	–0.198

the CCD. A combination of one flat-field spectral exposure with one bright-calibration star spectrum was used to trace the spatial ends of the slit for each of the 10 curved echelle orders. Scattered light was subtracted from individual frames by fitting a smooth function. During the July 2001 Keck II run, two spectra were taken for all the 13 objects observed. The frames were combined and cosmic rays removed as described before. Moreover, to remove the cosmic rays from the single frames of run #8 and #10 (Table C.1), we used the LA_Cosmic task (van Dokkum 2001). To preserve spatial information, the *apall* task was used in *strip* mode to extract and rectify two-dimensional rectangular strips for each echelle order. Scientific data, flat field, arc lamp, and standard stars exposures were extracted and rectified using the same procedure. The final results of the extraction were 10 two-dimensional spectra for every frame. They were reduced using the same procedure as used for long-slit spectra and described before. Each strip was divided by its corresponding flat-field frame and then it was wavelength-calibrated. The calibration was done with a combination of Cu/Ar/Hg/Ne arc lamp spectra for the orders from 7 to 15. In the order 6 both the lamp spectrum and the ESI sky emission lines atlas do not cover the entire extension of the strip. For the calibration of this order, we used the ESI sky atlas combined with some sky lines taken from Rousselot et al. (2000).

The goodness of the calibration was again checked measuring the wavelength of some emission sky lines, where possible (from the 6th to the 12th order). The errors are less than 3 km s^{-1}. The rms of the residuals in the wavelength solution is less than 0.09 Å for the 6th order and 0.07 Å for the others.

Table C.1. Redshifts of IDS/ISOCAM galaxies.

Name	RA (2000)	Dec (2000)	Spectral run[a]	Imaging run[b]	z	B	R	Complete sample? (y/n)
3-01A	17 47 24.74	67 26 48.3	–	1	star	–	–	n
3-03A	17 48 00.51	66 32 17.9	–	1	–	17.15 ± 0.01	16.03 ± 0.05	y
3-04A1	17 48 03.72	66 56 31.0	7	5	0.1180	18.03 ± 0.02	16.99 ± 0.03	y
3-04A2	17 48 04.01	66 56 26.9	7	5	0.1176	19.58 ± 0.03	18.10 ± 0.03	y
3-05A	17 48 00.51	66 28 41.8	–	1	–	15.54 ± 0.02	14.30 ± 0.01	y
3-07A	17 48 27.11	66 14 05.9	–	1	–	17.67 ± 0.01	16.33 ± 0.01	y
3-08A1	17 48 37.6	67 41 57.6	–	1	–	16.93 ± 0.02	15.37 ± 0.01	y
3-08A2	17 48 35.7	67 41 56.3	–	1	–	19.39 ± 0.02	18.39 ± 0.01	y
3-09A	17 48 50.44	66 53 55.3	–	1	–	15.96 ± 0.02	14.55 ± 0.01	n
3-10A1	17 49 22.61	66 25 53.6	1,3	1	0.0875	17.27 ± 0.01	16.42 ± 0.08	y
3-10A2	17 49 21.74	66 25 52.3	1,3	1	0.0867	18.57 ± 0.01	17.30 ± 0.02	y
3-11A	17 49 15.21	67 20 12.8	9	–	0.0236	–	–	y
3-12A	17 49 33.72	66 51 22.9	3	–	0.0775	–	–	y
3-13A	17 49 32.55	67 26 56.9	7	–	0.364*	–	–	n
3-14A	17 50 30.97	65 38 11.9	7	1	0.0426	17.91 ± 0.02	16.44 ± 0.01	y
3-16A	17 50 25.01	67 00 08.7	8	–	0.1176	–	–	y
3-17A	17 50 26.69	66 48 22.7	7	2	star	–	–	n
3-17B	17 50 34.62	66 48 28.4	7	2	0.0702	19.32 ± 0.02	17.66 ± 0.02	n
3-18A	17 51 04.04	67 47 20.1	–	1	star	–	–	n
3-19A	17 51 37.58	65 33 48.9	6	1	0.0520	17.40 ± 0.12	15.57 ± 0.08	y
3-19B	17 51 31.98	65 33 43.4	–	1	star	–	–	n
3-19C	17 51 30.04	65 34 12.8	6	1	0.0444	17.50 ± 0.06	15.75 ± 0.03	n
3-20A	17 51 17.97	67 12 31.7	3	–	0.0736	–	–	y
3-20B	17 51 15.95	67 12 02.4	9	–	star	–	–	n
3-21A	17 52 20.76	66 25 56.1	7	5	0.0523	17.44 ± 0.09	16.56 ± 0.07	n
3-23A	17 52 53.37	65 30 05.9	7	5	0.0877	18.25 ± 0.08	16.96 ± 0.07	n
3-24A	17 53 48.14	66 39 23.9	3	–	0.1164	–	–	y
3-26A	17 54 38.39	66 23 21.5	10	1	0.0894	18.41 ± 0.01	17.09 ± 0.01	y
3-26B	17 54 37.38	66 22 46.3	10	1	0.0889	18.05 ± 0.01	16.88 ± 0.05	y
3-26C	17 54 47.20	66 23 19.4	4	1	0.0885	17.91 ± 0.02	16.57 ± 0.01	n
3-26D	17 54 45.44	66 23 50.2	4	1	0.0874	18.04 ± 0.08	16.67 ± 0.04	n
3-27A	17 54 46.19	66 48 25.5	3,7	5	0.0876	17.75 ± 0.01	16.22 ± 0.01	y
3-27B	17 54 39.44	66 49 25.1	7	5	0.0868	18.06 ± 0.09	16.83 ± 0.01	n
3-28A	17 54 57.91	65 54 06.2	–	1	–	15.60 ± 0.02	14.60 ± 0.01	n
3-29A	17 54 55.75	66 13 11.2	3	–	0.0408	–	–	n
3-30A	17 54 51.18	67 09 50.2	8	–	0.2545	–	–	n
3-31A	17 55 18.10	66 32 23.6	7	5	0.0267	14.79 ± 0.01	13.58 ± 0.08	y
3-32A	17 55 33.77	65 57 04.5	4,5	1	0.0371	16.98 ± 0.01	15.67 ± 0.01	n
3-32B	17 55 11.67	65 56 54.5	5	1	0.042*	15.71 ± 0.06	14.15 ± 0.04	n
3-33A1	17 55 21.3	66 24 26.1	4	2	0.1445	18.90 ± 0.01	17.57 ± 0.10	n
3-33A2	17 55 21.4	66 24 25.5	–	2	–	21.56 ± 0.02	19.97 ± 0.08	n
3-33A3	17 55 22.0	66 24 29.4	–	2	–	22.31 ± 0.01	20.89 ± 0.05	n
3-33B	17 55 20.12	66 23 03.4	–	2	star	–	–	n
3-36A	17 55 45.34	67 47 53.9	8	5	0.1183	19.59 ± 0.03	17.74 ± 0.01	y
3-36B	17 55 49.09	67 46 56.2	7	5	0.0852	16.52 ± 0.06	14.92 ± 0.09	n
3-37A	17 55 55.12	67 20 07.7	3	–	0.0507	–	–	y
3-38A	17 56 06.55	66 47 39.2	7	5	0.0883	17.78 ± 0.04	16.33 ± 0.07	n
3-38B	17 56 15.31	66 46 50.3	7	5	0.0880	16.97 ± 0.01	15.44 ± 0.02	n
3-39A1	17 56 07.7	67 43 48.3	2	3	0.1179	–	17.46 ± 0.04	n
3-39A2	17 56 08.9	67 43 48.9	–	3	–	–	19.55 ± 0.02	n
3-40A	17 56 26.95	67 23 58.3	3	–	0.0892	–	–	y
3-40B	17 56 36.41	67 24 23.9	3	–	2.953	–	–	n
3-41A	17 56 39.72	66 48 00.3	–	5	–	17.22 ± 0.13	16.15 ± 0.14	y

Table C.1. continued.

Name	RA (2000)	Dec (2000)	Spectral run[a]	Imaging run[b]	z	B	R	Complete sample? (y/n)
3-42A	17 56 52.25	65 46 08.5	7	5	0.1383	18.28 ± 0.04	16.64 ± 0.02	n
3-44A1	17 57 31.6	67 19 55.9	3	4	0.2211	21.19 ± 0.04	–	n
3-44A2	17 57 31.6	67 20 00.2	3	4	0.3027	21.87 ± 0.02	–	n
3-44A3	17 57 32.1	67 19 55.8	–	4	–	–	–	n
3-45A	17 57 32.61	67 45 53.5	10	–	0.0791	–	–	y
3-47A	17 58 11.64	65 28 35.4	7	5	0.0874	18.48 ± 0.28	16.91 ± 0.68	y
3-48A	17 58 17.29	65 39 05.1	–	3	–	–	14.93 ± 0.01	y
3-49A1	17 58 16.4	65 52 36.5	2	3	0.0407	–	18.42 ± 0.02	n
3-49A2	17 58 16.5	65 52 34.7	–	3	–	–	18.83 ± 0.04	n
3-51A	17 58 38.64	65 40 31.5	2	3	0.1108	–	17.43 ± 0.08	y
3-51B	17 58 41.85	65 38 54.0	–	3	–	–	18.74 ± 0.11	n
3-53A1	17 58 30.7	67 44 06.9	3	4	0.3723	20.07 ± 0.02	–	y
3-53A2	17 58 30.9	67 43 58.8	3	4	star	19.89 ± 0.01	–	y
3-53A3	17 58 29.9	67 44 11.7	3	4	–	22.44 ± 0.03	–	y
3-53A4	17 58 32.6	67 44 11.3	3	4	–	21.59 ± 0.01	–	y
3-54A1	17 58 50.1	66 07 14.8	2	3	0.0797	–	17.03 ± 0.10	n
3-54A2	17 58 49.6	66 07 14.0	–	3	–	–	21.78 ± 0.51	n
3-55A	17 58 47.13	66 48 01.0	2	3	0.0775	–	17.20 ± 0.19	n
3-56A	17 58 47.44	67 15 54.9	7	5	0.0891	16.11 ± 0.04	14.83 ± 0.03	y
3-57A1	17 59 05.55	66 16 04.8	2	3	0.0885	–	16.69 ± 0.02	y
3-57A2	17 59 05.52	66 16 11.7	2	3	0.0889*	–	19.13 ± 0.03	n
3-58A	17 59 09.05	66 25 14.4	2	3	0.0876	–	16.49 ± 0.02	n
3-59A	17 59 18.64	66 06 37.5	2	3	0.0865	–	16.74 ± 0.06	n
3-61A	18 00 08.36	67 27 41.7	2	3	0.0545	–	14.94 ± 0.06	y
3-63A	18 00 56.06	67 21 34.7	–	3	–	–	16.27 ± 0.01	y
3-64A	18 01 07.02	67 25 32.7	2,4	3	0.0119	–	13.42 ± 0.01	y
3-65A1	18 01 27.17	67 00 55.1	3	4	0.1667	19.35 ± 0.01	–	y
3-65A2	18 01 28.29	67 00 46.1	3	4	0.1672	20.60 ± 0.01	–	y
3-66A	18 01 50.02	66 59 14.4	10	–	0.0536	–	–	y
3-68A	18 01 45.36	67 09 00.6	2	3	0.0380*	–	14.63 ± 0.13	n
3-69A	18 02 48.59	67 00 12.3	10	–	0.1043	–	–	n
3-70A	18 03 01.41	66 23 49.8	10	–	0.1970	–	–	y
3-71A	18 03 21.03	66 50 41.6	10	–	0.0516	–	–	n
3-72A	18 03 24.77	67 31 38.1	9	–	star	–	–	n
3-73A	18 03 41.99	67 03 06.6	2,4	3	0.0269	–	13.88 ± 0.01	y
3-75A	18 04 07.32	67 29 32.8	8	–	0.1725	–	–	n
3-76A	18 04 27.13	67 20 45.4	10	–	0.0800	–	–	n
3-77A	18 04 52.78	65 50 01.9	2	3	0.0864	–	17.29 ± 0.01	y
3-78A	18 05 08.13	67 08 54.6	2	3	0.0884	–	17.35 ± 0.01	n
3-78B	18 05 09.56	67 07 42.6	2	3	0.0781	–	17.89 ± 0.15	n
3-78C1	18 05 07.9	67 07 14.1	8	3	0.2610	–	19.04 ± 0.01	n
3-78C2	18 05 06.7	67 07 19.1	8	3	0.2611	–	19.01 ± 0.01	n
3-78C3	18 05 09.5	67 07 09.9	–	3	–	–	21.17 ± 0.05	n
3-79A	18 05 17.61	66 54 04.2	7	5	0.0589	16.97 ± 0.03	15.30 ± 0.11	y
3-79B	18 05 25.03	66 54 48.6	–	5	star	–	–	n
3-79C	18 04 59.66	66 54 48.2	7	5	0.0538	18.02 ± 0.01	16.86 ± 0.01	n
3-80A	18 05 14.89	67 12 21.6	–	5	star	–	–	n
3-80B	18 05 16.81	67 12 03.8	–	5	–	–	16.44 ± 0.01	y
3-81A	18 05 28.22	65 54 34.8	2	5	0.0282	–	14.65 ± 0.01	y
3-81B	18 05 36.59	65 54 08.9	2	5	0.0264	–	16.30 ± 0.10	n
3-83A1	18 06 27.58	66 20 17.4	10	4	0.1071	19.91 ± 0.01	–	y
3-83A2	18 06 25.66	66 20 20.1	10	4	0.1071	19.59 ± 0.01	–	y
3-84A1	18 06 40.0	66 32 40.9	7	5	0.0860	18.84 ± 0.03	17.43 ± 0.03	y
3-84A2	18 06 38.6	66 32 35.7	–	5	–	19.52 ± 0.01	18.06 ± 0.01	y

Table C.1. continued.

Name	RA (2000)	Dec (2000)	Spectral run[a]	Imaging run[b]	z	B	R	Complete sample? (y/n)
3-85A1	18 07 18.0	67 02 04.6	7	5	0.1505	–	16.57 ± 0.01	y
3-85A2	18 07 19.1	67 02 04.4	7	5	–	–	17.79 ± 0.02	y
3-86A	18 07 39.78	65 34 15.8	7	–	star	–	–	n
3-88A1	18 09 13.0	66 12 52.8	7	5	0.0516	17.28 ± 0.01	16.80 ± 0.01	y
3-88A2	18 09 12.2	66 12 48.9	–	5	–	19.82 ± 0.07	18.50 ± 0.08	y
3-88B	18 09 23.53	66 12 56.1	–	5	star	–	–	n
3-89A1	18 09 20.53	67 34 11.5	3	4	0.2996	21.68 ± 0.01	–	y
3-89A2	18 09 21.23	67 34 10.9	3	4	0.2992	22.97 ± 0.05	–	y
3-90A	18 09 37.41	66 49 59.8	10	–	0.0721	–	–	y
3-91A	18 09 51.87	67 08 52.4	7	5	0.0686	17.38 ± 0.01	16.62 ± 0.05	n
3-92A	18 10 24.42	66 42 56.9	2	3	0.0887	–	17.43 ± 0.01	n
3-92B	18 10 18.54	66 43 11.6	–	3	star	–	–	n
3-92C	18 10 24.87	66 42 15.4	2	3	0.0887	–	17.45 ± 0.02	n
3-93A	18 10 34.46	66 11 17.1	2	3	0.0691	–	16.28 ± 0.01	y
3-96A	18 10 54.05	67 45 16.6	10	–	0.3525	–	–	y

[a] The spectroscopic runs #1 (June 00), #4 (August 01), #6 (October 03) , and #9 (June 02) were performed at the Cima Ekar 1.82 m telescope + AFOSC; #2 (May 01) and # 7 (June 02) at the TNG + DOLORES; #8 (June 02) and #10 (September 02) at Keck II + ESI.
[b] The imaging runs #1 (April 00) and #2 (May 00) were performed at the TNG + OIG; #3 (May 01) and # 5 (June 02) at the TNG + DOLORES; #4 (July 01) at Keck II + ESI.